




## Low thermal conductivity and semimetallic behavior in some TiNiSi structure-type compounds

Kumar Saurabh , Ankit Kumar , Prasenjit Ghosh , and Surjeet Singh \*

Department of Physics, Indian Institute of Science Education and Research, Dr. Homi Bhabha Road, Pune 411 008, India



(Received 12 May 2021; accepted 2 August 2021; published 23 August 2021)

Motivated by recent advances in half-Heusler based thermoelectric materials, we investigated the phase stability and thermoelectric properties of compounds ZrNiSi, ZrNiGe, HfNiSi, NbCoSi, and ZrNiSb, some of which were recently reported in literature as promising half-Heuslers for thermoelectric applications using the first-principles density functional theory based calculations. Here, we show that all the named compounds actually crystallize with the orthorhombic TiNiSi structure type, which remains stable above room temperature up to at least 1100 K. In ZrNiSb, 5% excess Zr is required to obtain the pure orthorhombic phase. Our first-principles electronic band structure calculations reveal that they are semimetals. In ZrNiSi, ZrNiGe, and HfNiSi, the Fermi surface consists of small electron and hole pockets with electrons as the majority charge carriers. In NbCoSi and ZrNiSb, the majority carriers are holes. A pseudogaplike feature is observed in the electronic density of states with Fermi energy ( $E_F$ ) located either slightly below (ZrNiSi, ZrNiGe, and HfNiSi) or above the pseudogap (NbCoSi). In ZrNiSb no pseudogap is observed; however, the density of states at  $E_F$  is still small. The electrical conductivity ( $\sigma$ ) near room temperature is of the order of  $10^3 \text{ S cm}^{-1}$ , which is intermediate between that of the degenerate semiconductors and metallic alloys. Near room temperature the thermopower is negative for ZrNiX ( $X = \text{Si, Ge}$ ) and HfNiSi, and positive for NbCoSi and ZrNiSb as predicted theoretically. The average value of Seebeck coefficient is small, of the order of  $10 \mu\text{V K}^{-1}$ . Despite reasonably high electrical conductivity, the thermal conductivity ( $\kappa$ ) of these compounds is found to be generally low ( $<15 \text{ W m}^{-1} \text{ K}^{-1}$  near 300 K). In  $\text{Zr}_{1.05}\text{NiSb}$ , which has the highest electrical conductivity ( $\approx 4000 \text{ S cm}^{-1}$ ),  $\kappa$  is as low as  $\approx 4 \text{ W m}^{-1} \text{ K}^{-1}$  at 300 K, of which almost 70% is estimated to be due to the electronic contribution resulting in a lattice contribution which is  $<1 \text{ W m}^{-1} \text{ K}^{-1}$ . This uncommon combination of high electrical conductivity and low thermal conductivity is interesting and invites further attention.

DOI: [10.1103/PhysRevMaterials.5.085406](https://doi.org/10.1103/PhysRevMaterials.5.085406)

### I. INTRODUCTION

The orthorhombic  $MTX$  family, where  $M$  is a transition metal,  $T$  is a late transition metal, and  $X$  is a main group element, constitute a very large class of intermetallic compounds crystallizing with the TiNiSi structure type. Recently, compounds of this structure class have attracted significant attention due to their interesting magnetostructural, transport, and thermodynamic properties, including giant magnetocaloric effect [1,2], cycloidal magnetic ordering [3], coexisting hexagonal and orthorhombic phases showing an interplay of planar and spiral magnetic ground states [4], and promising thermoelectric properties [5]. In a recent work, a novel nodal-line topological phase was proposed for several members of this family based on the first-principles electronic structure calculations [6].

The compound TiNiSi has an orthorhombic symmetry (space group  $Pnma$ , Pearson symbol oP12) as shown in Fig. 1(a). The structure consists of corrugated 2D sheets of edge-sharing  $\text{Ni}_3\text{Si}_3$  hexagonal rings stacked along the  $a$  axis [Figs. 1(b) and 1(d)] of the orthorhombic unit cell. When viewed along the  $b$  axis, a distinctive chair-shaped ... Si–Ni–Si–Ni ... framework running parallel to the  $a$  axis with

Si–Ni–Si bond angle close to  $110^\circ$  can be seen [see Fig. 1(c)]. A similar structural architect in SnSe has been argued as one of the factors responsible for its ultralow thermal conductivity [7]. In the TiNiSi structure, while the Ti atoms are fivefold coordinated by Si, the coordination of Ni atoms is fourfold, forming a distorted  $\text{NiS}_4$  tetrahedron [Fig. 1(a)].

The quest for high-performance thermoelectric materials in this family has recently led to several high-throughput computational studies to evaluate their potential as efficient thermoelectrics [8–12]. In several of these studies, the  $MTX$  compounds have been identified with the cubic half-Heusler (hH) structure, and promising thermoelectric properties have been predicted, including a high power factor of  $400 \mu\text{W cm}^{-1} \text{ K}^{-2}$  ( $p$  type) and  $650 \mu\text{W cm}^{-1} \text{ K}^{-2}$  ( $n$  type) for hH NbCoSi [8]. The hH phase is often considered in such calculations as it is argued to be more stable at low temperatures. However, if the vibrational entropy is also considered explicitly, as done recently by Guo *et al.* [13], who considered the vibrational contribution to the Gibbs free energy in their first-principles calculations, then the hexagonal or orthorhombic phases become energetically favorable.

The experimental effort towards synthesizing and evaluating the phase stability and thermoelectric properties of these compounds has been limited so far. Recently, Huang *et al.* reported the thermoelectric properties of TiNiSi with V doping at the Ti site [14]. They reported a maximum thermopower

\*Corresponding author: Surjeet.singh@iiserpune.ac.in

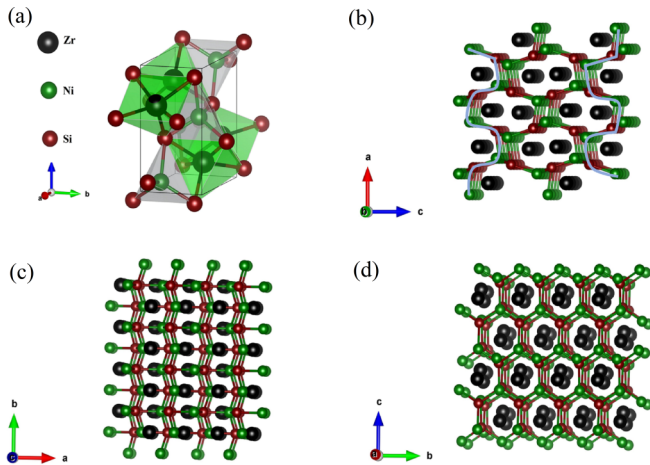


FIG. 1. Crystal structure of TiNiSi structure-type ZrNiSi. (a) Orthorhombic unit cell showing the coordination of Zr and Ni by Si. The crystal structure as viewed along the (b)  $b$  axis, (c)  $c$  axis, and (d)  $a$  axis is shown (see text for details).

of  $-43 \mu\text{V K}^{-1}$  at 560 K for a sample doped with 20% vanadium. In CaAgSb, which crystallize in the same TiNiSi structure type, a thermoelectric figure of merit ( $zT$ ) of 0.1 was previously reported that was shown to increase dramatically to  $zT = 0.7$  upon Ce doping for Ca with simultaneous Ag vacancies to retain the valence balanced condition [15]. Here,  $zT$  is a dimensionless quantity given by  $zT = \frac{\sigma S^2 T}{\kappa}$  (where  $\sigma$ ,  $S$ , and  $\kappa$  represents electrical conductivity, Seebeck coefficient, and thermal conductivity, respectively, and  $T$  is absolute temperature in K), which is a measure of the goodness of a material for thermoelectric applications [16, 17]. It is therefore believed that orthorhombic  $MTX$  compounds may provide an alternative avenue for realizing efficient high-temperature thermoelectrics. Their proximity to the related higher symmetry hexagonal and cubic (hH) phases further enhances this possibility [8, 13, 18].

In this work, we report the electronic structure, synthesis, structural characterizations, and thermoelectric properties of the compounds ZrNiSi, HfNiSi, ZrNiGe, NbCoSi, and ZrNiSb. We show that all the studied compounds crystallize with the orthorhombic TiNiSi structure type. While ZrNiSi, HfNiSi, ZrNiGe, and NbCoSi (nominal valence electron count 18) form readily upon arc melting, ZrNiSb (nominal valence electron count 19) forms but with precipitous amounts of secondary phases which can be suppressed by taking 5% excess Zr (hereafter, for this sample we shall use ‘ZrNiSb’ or  $\text{Zr}_{1.05}\text{NiSb}$  interchangeably).

The first principles electronic band structure calculations reveal that these compounds are semimetals with a pseudogap in their density of states except ZrNiSb, which appears more metal-like with a substantially large hole Fermi surface compared to that due to electrons. While the Fermi level ( $E_F$ ) is located slightly above the pseudogap in ZrNiX ( $X = \text{Si, Ge}$ ) and HfNiSi with electrons as the majority carriers, it is located below the pseudogap in NbCoSi, where the majority carriers are holes. The sign of experimentally measured Seebeck coefficient is found to be in agreement with this assessment. The measured electrical conductivity ( $\sigma$ ) of our samples near

300 K ranged from  $\approx 1000 \text{ S cm}^{-1}$  (ZrNiSi) to  $\approx 4000 \text{ S cm}^{-1}$  (ZrNiSb). These values are intermediate between those of degenerate semiconductors and metallic alloys, in line with their semimetallic behavior inferred from the first-principles calculations. The thermal conductivity ( $\kappa$ ) of these samples is found to be generally low, varying from  $\approx 15 \text{ W m}^{-1} \text{ K}^{-1}$  (ZrNiSi) to as low as  $\approx 4 \text{ W m}^{-1} \text{ K}^{-1}$  (ZrNiSb) near 300 K. The lattice thermal conductivity ( $\kappa_l$ ) of ZrNiSb, in particular, is found to be very low ( $\sim 1 \text{ W m}^{-1} \text{ K}^{-1}$ ) near 300 K despite its highest electrical conductivity.

The rest of the paper has been organized as follows. The experimental and computational details are presented in Sec. II. This is followed by results and discussion in Sec. III. For the ease of reading, this section has been further structured as follows. Synthesis and structural characterizations are covered under Sec. III A. Within this, the compounds ZrNiSi, HfNiSi, ZrNiGe, and NbCoSi are presented in Sec. III A 1 and ZrNiSb separately in Sec. III A 2. After furnishing the experimental structural details, we present our theoretical calculations under Sec. III B. This is followed by a section dealing with the experimental assessment of thermoelectric properties and their comparison with the theoretical results (Sec. III C), with electrical transport under Sec. III C 1 and thermal conductivity under Sec. III C 2. The summary and conclusions drawn from this work appear under Sec. IV.

## II. EXPERIMENTAL AND COMPUTATIONAL DETAILS

### A. Experimental details

Samples were synthesized using the arc-melting technique under a high-purity argon gas. Stoichiometric amounts of Zr (Sigma Aldrich,  $\geq 99\%$ ), Nb (Sigma Aldrich,  $\geq 99.9\%$ ), Co (Sigma Aldrich, 99.5%), Ni (Sigma Aldrich,  $\geq 99.9\%$ ), Si (Sigma Aldrich, 99.5%), Sn shots (Sigma Aldrich, 99.8%), Hf pieces (Sigma Aldrich, 99.7% trace metal basis), and Sb shots (Alfa Aesar,  $\geq 99.999\%$ ) were used. The starting precursors were weighed according to the required stoichiometry and loaded on the water cooled copper hearth of the arc furnace. The chamber was evacuated and purged with a high-purity argon gas repeatedly for several times before striking the arc. A zirconium getter was used to absorb any remnant oxygen in the chamber. The ingot was flipped over and re-melted five to six times to ensure a good homogeneity. For the synthesis of ZrNiSi, ZrNiGe, HfNiSi, and NbCoSi, the starting precursors were taken in the molar ratio 1 : 1 : 1. In the case of ZrNiSb, a total of six samples with nominal composition  $\text{Zr}_{1-x}\text{NiSb}$  ( $x = -0.05, 0, 0.05, 0.1, 0.15, \text{ and } 0.25$ ) were synthesized. In each case, approximately 10% extra Sb was added to compensate for the Sb loss during melting. The amount of excess Sb to be added was estimated by weighing the ingot before and after arc melting at a fixed power and for a fixed duration. The arc-melted ingot of  $\text{Zr}_{1.05}\text{NiSb}$  (or ‘ZrNiSb’), which is the only sample that forms as nearly single phase, was cut into two parts. The smaller part was crushed into fine powder by hand grinding in air using an agate mortar and pestle, and subsequently pelletized using a KBr press. The pressed pellet was annealed at  $900^\circ\text{C}$  for 6 days in a vacuum-sealed quartz tube coated inside with a thin layer of carbon to avoid the pellet from reacting with silica. The physical properties were

measured only on the as-melted sample. For this purpose, the arc-melted ingots were cut using a low-speed diamond saw (South Bay, USA) into a disk shaped specimen for the measurement of thermal conductivity and a rectangular bar shaped specimen for resistivity and thermopower.

To check the phase formation and presence of secondary phase(s), if any, powder x-ray diffraction was done at various stages of the sample synthesis (Bruker, D8 Advance). The lattice parameters were obtained by least-square refinement using the UNITCELL program. Polished specimens cut from the as-melted ingots were also examined using a Field Effect Scanning Electron microscope (FESEM) (Ultra Zeiss plus), equipped with an Energy Dispersive X-ray (EDX) analysis attachment (Oxford Instruments). The resistivity and thermopower were measured simultaneously using the Linseis LSR-3 setup. The average uncertainties in these measurements are less than 5%. The thermal diffusivity ( $D$ ) was measured using the Linseis LFA-1000 instrument on polished disks that were homogeneously coated with a very thin layer of graphite. The average uncertainty in thermal diffusivity using this setup is near 5%. Thermal conductivity ( $\kappa$ ) was obtained from the thermal diffusivity by the formula  $\kappa = D \rho C_p$ , where  $\rho$  is the mass density and  $C_p$  is the specific heat for which we used the value corresponding to the Dulong-Petit limit ( $3nR = 74.8 \text{ J mol}^{-1} \text{ K}^{-1}$ ). While this may be a little overestimation, especially near room temperature, we used this to get an upper bound on  $\kappa$ . For mass density, we used the sample dimensions and sample mass, both of which were reasonably accurately accessible. The arc-melted ingots were free of micropores as revealed in the electron and optical microscope images of the polished specimens. The mass density is estimated to be close to 95% for all the samples. The  $\text{Zr}_{1.05}\text{NiSb}$  specimen turned porous after the annealing treatment; however, the physical properties were measured only for the as melted sample. HRTEM (JEOL JEM 2200FS 200 keV) was used to collect high-resolution images and for obtaining SAED patterns with the GSM-3 software package to assess the crystallinity of our samples. For examining the sample under the HRTEM, a piece of ingot was hand grinded into a fine powder, which was transferred onto a TEM Cu grid in an ethanol based solution that was oven dried at  $50^\circ\text{C}$  for close to an hour. The Cu grid was subsequently loaded on the TEM sample stage and plasma cleaned at 250 eV for about 15 min.

### B. Computational details

The first-principles calculations were done using the QUANTUM ESPRESSO software [19,20], which is a plane wave based implementation of density functional theory (DFT). Since the materials contain  $d$ -block elements, we have used the spin polarized form of DFT. The electron-ion interactions have been described using ultrasoft pseudopotential [21]. The valence configuration  $4s^2 5s^2 4p^6 4d^2$ ,  $4s^2 3d^8$ ,  $3s^2 3p^2$ ,  $5s^2 6s^2 5p^6 5d^2$ ,  $4s^2 5s^2 4p^6 4d^3$ ,  $4s^1 3d^8$ ,  $4s^2 4p^2$ ,  $5s^2 5p^3$  has been used for Zr, Ni, Si, Hf, Nb, Co, Ge, and Sb, respectively. We have used Perdew-Burke-Ernzerhof parametrization of the generalized gradient approximation (GGA-PBE) to describe the electron-electron exchange and correlation interactions [22]. The electronic wave functions are expanded in a plane wave

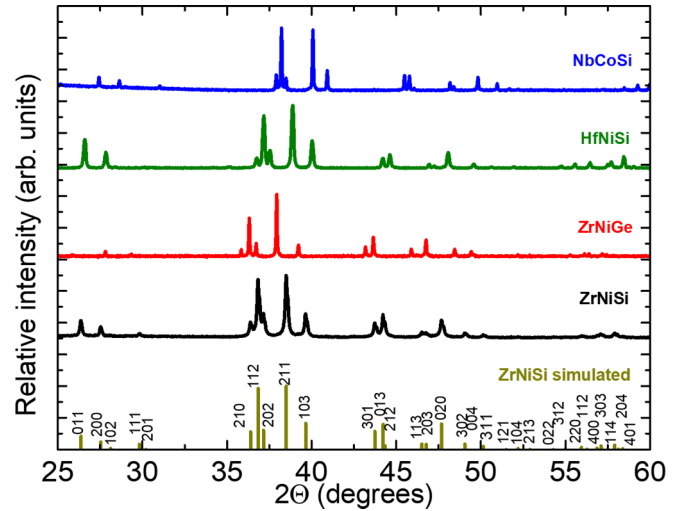


FIG. 2. Powder x-ray diffraction pattern of arc-melted ZrNiSi, ZrNiGe, HfNiSi, and NbCoSi samples. A simulated powder x-ray diffraction pattern for ZrNiSi (TiNiSi structure type) is also shown for comparison.

basis with kinetic energy cutoffs of 50 Ry for all the compounds except NbCoSi. For the latter, a cutoff of 55 Ry was used. For expanding the charge density, we have used a kinetic energy cutoff that is ten times that used for the wave function. A  $8 \times 16 \times 8$  Monkhorst-Pack  $k$ -point mesh was used for Brillouin zone integrations [23]. To speed up convergence we have used Marzari-Vanderbilt smearing with a smearing width of 0.03 Ry. Since it is known from the experimental data that all the studied compounds exhibit an orthorhombic structure with space group  $Pnma$ , in our calculations we have therefore considered only the orthorhombic structure. Experimental lattice parameters were used as input for structure optimization.

## III. RESULT AND DISCUSSION

### A. Structural characterization

#### 1. ZrNiSi, HfNiSi, ZrNiGe, and NbCoSi

The powder x-ray diffraction patterns of our arc-melted ZrNiSe, ZrNiGe, HfNiSi, and NbCoSi samples are shown in Fig. 2. The observed pattern can be satisfactorily indexed based on the orthorhombic TiNiSi structure type. In particular, no trace of secondary phases could be detected in any of the patterns shown. Thus the samples are single phase within the detection limit of this technique. The lattice parameters are shown in Table I. As expected, the unit cell volume of ZrNiGe is larger than that of ZrNiSi owing to the larger ionic radius of Ge compared to Si. Between ZrNiSi and HfNiSi, the Hf analog has smaller lattice parameters, which can be attributed to the lanthanide contraction. A similar relationship between the cell parameters of Zr and Hf analogs was previously reported for the ternary silicates  $M_2\text{Cr}_4\text{Si}_5$  ( $M = \text{Ti, Zr, and Hf}$ ) [24]. NbCoSi has the smallest lattice parameter owing to a much smaller size of Nb compared to either Zr or Hf.

Few representative backscattered FESEM micrographs for each of the four samples ZrNiSi, ZrNiGe, HfNiSi, and NbCoSi are shown in Fig. S1 in the Supplemental

TABLE I. Lattice parameters of various orthorhombic *MTX* compounds as obtained experimentally and using the DFT calculations.

Samples	Experimental			Vol ( $\text{\AA}^3$ )	Calculated			Vol ( $\text{\AA}^3$ )	Reference
	<i>a</i> ( $\text{\AA}$ )	<i>b</i> ( $\text{\AA}$ )	<i>c</i> ( $\text{\AA}$ )		<i>a</i> ( $\text{\AA}$ )	<i>b</i> ( $\text{\AA}$ )	<i>c</i> ( $\text{\AA}$ )		
ScNiSi	6.407	4.007	6.970	178.9					[25]
TiNiSi	6.152	3.671	7.021	158.5					[26]
ZrNiSi	6.472	3.812	7.276	179.5	6.485	3.810	7.299	180.3	This work
HfNiSi	6.400	3.782	7.214	174.6	6.415	3.787	7.214	175.2	This work
ZrNiGe	6.496	3.944	7.356	188.5	6.584	3.899	7.398	189.9	This work
NbCoSi	6.141	3.761	7.073	163.4	6.239	3.657	7.051	160.8	This work
'ZrNiSb'	6.732	4.153	7.490	209.4	6.765	4.172	7.667	216.4	This work

Material [27]. The chemical mapping for individual elements is also shown, which reflects a homogenous distribution of the constituents, corroborating their single-phase nature. The elemental molar ratio as determined using the EDX probe is  $\text{Zr}_{36.0}\text{Ni}_{31.7}\text{Si}_{32.2}$ ,  $\text{Zr}_{37.3}\text{Ni}_{31.4}\text{Ge}_{31.3}$ ,  $\text{Hf}_{30.4}\text{Ni}_{30.4}\text{Si}_{39.1}$ , and  $\text{Nb}_{35.9}\text{Co}_{31.1}\text{Si}_{33.0}$ . These indicate some deviations from actual composition, which is particularly noticeable in HfNiSi, whose EDX composition suggests  $\text{Hf}_{1-x}\text{Ni}_{1-x}\text{Si}_{1+2x}$  to be the chemical formula with possible compositional disorder at all three crystallographic sites. It should be emphasized that, even though the EDX composition of HfNiSi is close to 3 : 3 : 4, the powder x-ray diffraction confirms that the crystal structure is still orthorhombic TiNiSi type as shown in Fig. 2. The presence of secondary Hf and Ni rich phases occasionally seen in the SEM micrographs might be related to the less Hf and Ni in the main phase (see Fig. S3, Supplemental Material [27]). Since the errors associated with the EDX probe can often be large (up to 5 at. %), to get a more accurate estimate of the compositional disorder in these materials, it will be useful to perform inductively coupled plasma mass spectrometry (ICP-MS).

A low-resolution TEM image of a ZrNiSi micrograin, on which further analysis is done, is shown in Fig. 3(a). A high-resolution TEM image is shown in panel (b). One can clearly see neatly lined-up lattice planes which indicate a high crystallinity of our sample. A fast Fourier transform (FFT) image is shown as an inset, where the *hkl* indices of some of the diffraction spots is also labeled. In Fig. 3(c), the selected area electron diffraction (SAED) pattern is shown, which is similar to the FFT image. The diffraction spots observed in SAED are rather sharp, which corroborates the high crystallinity of the sample.

## 2. ZrNiSb

In analogy with the hH compounds, the compounds ZrNiSi, HfNiSi, ZrNiGe, and NbCoSi can be thought of as having a formal valence electron count (VEC) of 18 where the closed-shell electronic structure typically results in a semiconducting behavior within the Zintl concept. On the other hand, ZrNiSb has a formal VEC of 19 [VEC = 4 (Zr) + 10 (Ni) + 5 (Sb) = 19]. We found that, when arc melted by taking Zr, Ni, and Sb in the stoichiometric ratio (with some extra Sb to compensate for the losses during melting; see Sec. II A), the orthorhombic ZrNiSb phase forms but with several parasitic phases present, unlike the other four compounds where the

phase formation happens readily during the arc melting. In order to obtain a phase pure ZrNiSb, attempts were made by changing the starting Zr composition (to change the VEC). Thus six different alloys with varying starting Zr stoichiometry were arc melted.

The powder x-ray diffraction pattern of our  $\text{Zr}_{1-x}\text{NiSb}$  samples is shown in Fig. 4, where the simulated patterns for ZrNiSb based on TiNiSi structure type is also shown. The x-ray pattern of stoichiometric ZrNiSb ( $x = 0$ ) shows, besides peaks due to the main phase, extra peaks which can be attributed to the secondary phases  $\text{Zr}_2\text{Sb}$  and  $\text{ZrNi}_2\text{Sb}$ . Upon decreasing the quantity of Zr in the starting precursors

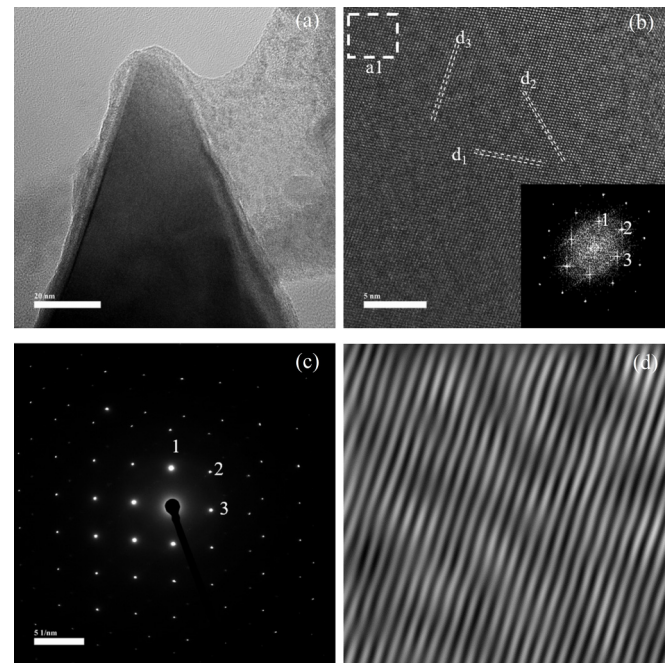


FIG. 3. TEM images of ZrNiSi sample: (a) a typical low-resolution TEM image showing a micrograin; (b) HRTEM image collected by focusing over a small portion of this micrograin. The dashed lines indicate some representative lattice planes: (103), (121), and (211) with interplanar spacing  $d_1 = 0.219$  nm,  $d_2 = 0.177$  nm, and  $d_3 = 0.237$  nm, respectively. The FFT is shown as an inset. (c) The SAED image showing sharp diffraction spots. The points labeled 1, 2, and 3 correspond to the lattice planes (103), (121), and (211); (d) zoomed-in IFFT of the square area marked as a1 in panel (b).

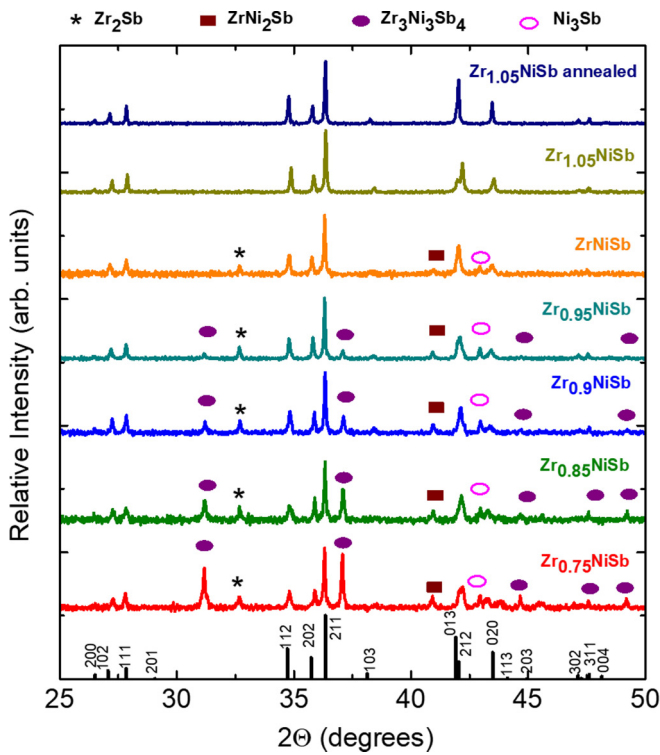


FIG. 4. Powder x-ray diffraction patterns for various arc-melted  $Zr_{1-x}NiSb$  ( $x = -0.05, 0, 0.05, 0.1, 0.15, 0.25$ ) and the annealed  $Zr_{1.05}NiSb$  are shown. The simulated pattern for the main  $ZrNiSb$  phase (TiNiSi structure type) is also shown. The peaks due to secondary phases  $ZrNi_2Sb$ ,  $Zr_3Ni_3Sb_4$ ,  $Zr_2Sb$ , and  $Ni_3Sb$  are also labeled.

( $x = 0.05$  and  $0.1$ ), the diffraction pattern remains nearly unchanged but the intensity of peaks due to secondary phases grew stronger and a new secondary phase, namely  $Zr_3Ni_3Sb_4$ , also emerged. Attempts to purify these samples by annealing at  $900\text{ }^\circ\text{C}$  for 6 days rather increased the  $Zr_3Ni_3Sb_4$  phase further at the expense of the  $ZrNiSb$  phase. We also arc melted a

sample corresponding to the stoichiometry  $Zr_{0.75}NiSb$  which should have a formal VEC of 18; this was done to check if it mimics the behavior of VEC 19 compound  $NbCoSb$ , which forms as a single phase when Nb concentration is close to 0.8 [28]. We found that  $Zr_{0.75}NiSb$  also does not form as a single phase sample, which, in a way, corroborates Landrum *et al.* [26], who suggested that the Zintl concept does not hold for these orthorhombics. On the other hand, we find  $Zr_{1.05}NiSb$  to be nearly phase pure. The x-ray diffraction pattern of our arc-melted sample shows only one small extra peak due to some unidentified phase near  $42^\circ$ , adjacent to the twin (013)/(212) peak of the main phase. However, upon annealing at  $900\text{ }^\circ\text{C}$  for 6 days even this extra peak disappeared, resulting in a phase pure sample.

In Fig. 5 representative FESEM images of arc-melted  $ZrNiSb$  and  $Zr_{1.05}NiSb$  specimens are shown. The presence of secondary phase(s) in  $ZrNiSb$  is reflected in the phase contrast image where the dark gray regions are seen embedded in the matrix of the main phase, whose average EDX composition was found to be  $Zr_{1.1}Ni_{0.8}Sb$ . The composition of the dark-gray region is  $Zr_{1.1}Ni_{1.9}Sb$ , which is close to that of the Heusler phase  $ZrNi_2Sb$ . In  $Zr_{1.05}NiSb$ , on the other hand, a much smaller precipitation is observed. The average composition of the main phase in this case is  $Zr_{38.3}Ni_{27.8}Sb_{33.9}$ . From these observations we can infer that the desired orthorhombic phase forms with nearly 5% excess Zr. It may be that some or all of this excess Zr resides at the Ni site. A chemical map for the elements Zr, Ni, and Sb in  $Zr_{1.05}NiSb$  is shown in Fig. S2 in the Supplemental Material [27], which suggests a homogeneous distribution of these elements.

Some representative HRTEM images of a  $Zr_{1.05}NiSb$  sample are shown in Fig. 6. As shown in panel (b), regions with well-defined arrays of lattice planes (one such region labeled a2 is shown) are interspersed by regions with defects (one such region labeled a1 is shown). The high crystallinity of a region such as a2 is corroborated by the presence of sharp diffraction spots in the SAED image shown as an inset. In panel (c), the inverse fast Fourier transform (IFFT) image of region a1 is shown. The presence of high density of stacking

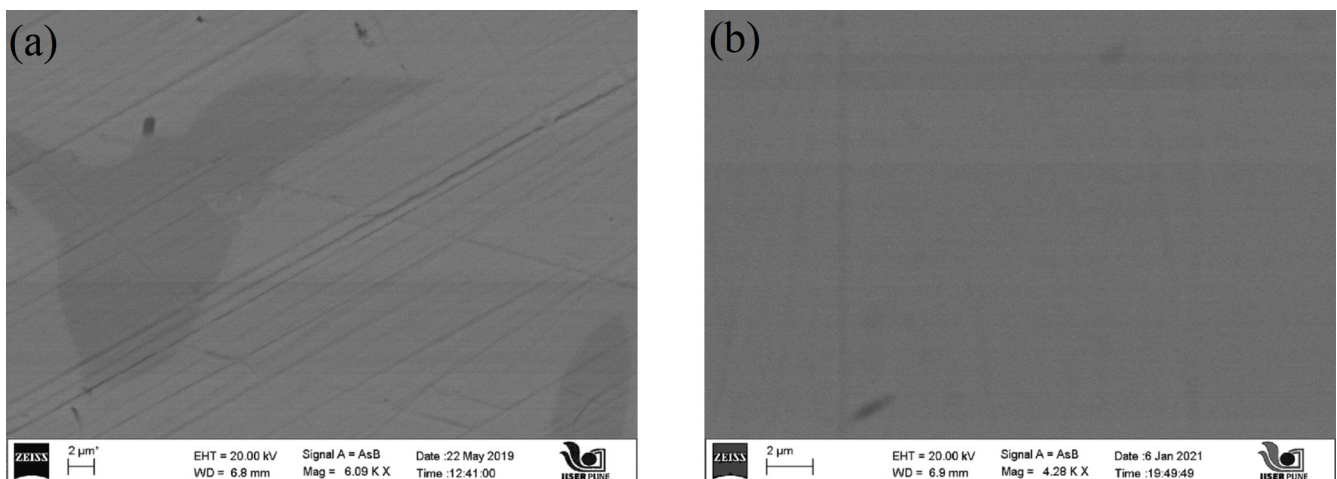


FIG. 5. Representative backscattered FESEM image each of  $ZrNiSb$  (left) and  $Zr_{1.05}NiSb$  (right). The dark gray regions in the image on the left are due to the impurity phase  $ZrNi_2Sb$ . The composition of the main matrix in both cases is close to  $Zr_{1.1}Ni_{0.83}Sb$ .

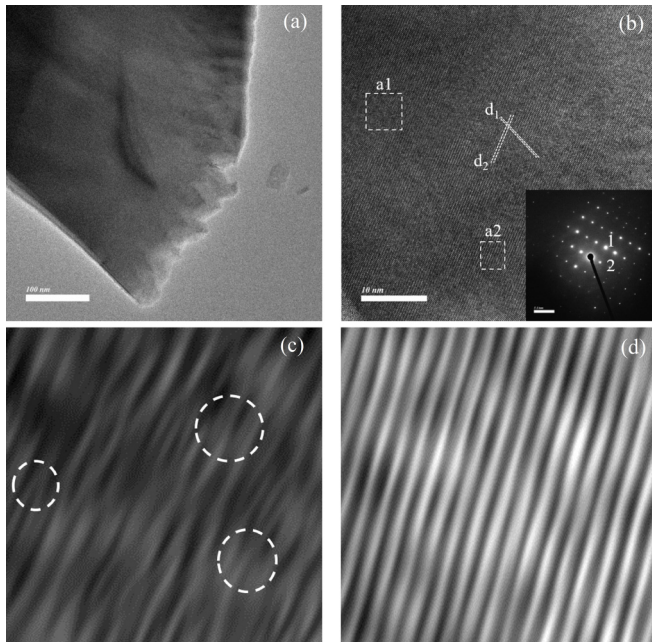


FIG. 6. TEM images of a  $Zr_{1.05}NiSb$  sample: (a) a low-resolution TEM image of a micrograin; (b) HRTEM image taken by focusing the electron beam on a small region of this micrograin. The lattice planes (013) and (011) are shown with interplanar spacing  $d_1 = 0.22$  nm (013) and  $d_2 = 0.36$  nm (011). The SAED image is shown as an inset where the points labeled 1 and 2 correspond to the lattice planes (011) and (013); (c) and (d) zoomed IFFT of the areas shown with white dashed lines marked as a1 and a2, respectively, in panel (b); circles have been drawn to show some of the stacking faults in the region a1 which are present in high density as compared to region a2.

faults due to merging or termination of the lattice planes can be clearly seen. In a similar image in panel (d) of region a2 such defects are not seen.

### B. Electronic structure calculations

In order to understand the electronic properties of these compounds we have performed DFT based calculations. The computed lattice parameters are in good agreement with the experimental values (see Table I). In typical hH, in the  $T-X$  network, each  $T$  is bound tetrahedrally with  $X$  and vice versa. These tetrahedrons are ideal with the four  $T-X$  bonds of equal length. However, for the  $MTX$  compounds considered in this study, we find that the  $T-X$  tetrahedrons are highly distorted (see Fig. S4 in the Supplemental Material); for each case, of the four  $T-X$  bonds, the two shortest bonds are of equal length but the two longer bonds have different bond lengths. The  $T-X$  bond lengths for the different compounds are listed in Table T1 in the Supplemental Material [27]. In a comparison of the bond lengths between  $ZrNiSi$  and  $ZrNiGe$  where one is moving down the Periodic Table with respect to  $X$ , we observe that all the  $T-X$  bond lengths increase. In contrast, when Zr is replaced with Hf in  $ZrNiSi$ , we observe that the two shortest  $T-X$  bonds have similar lengths (2.36 Å in  $ZrNiSi$  vs 2.35 Å in  $HfNiSi$ ) while the length of the other two long bonds has been reduced. In order to understand the nature of the bonding

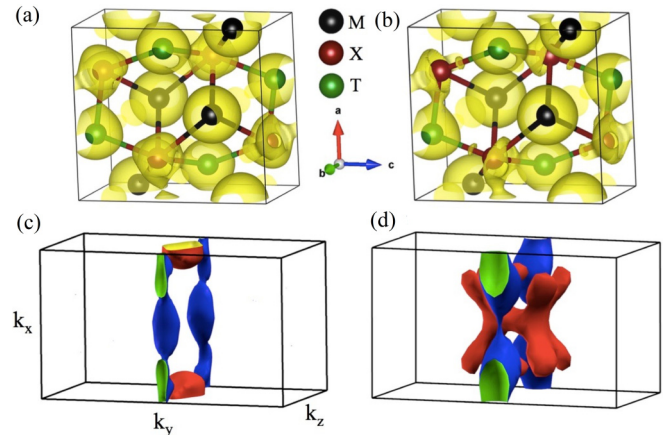


FIG. 7. Charge density isosurfaces of (a)  $ZrNiSi$  and (b)  $NbCoSi$ . The isovalues corresponding to these plots are 0.398 and 0.438  $e/\text{Å}^3$  for  $ZrNiSi$  and  $NbCoSi$ , respectively. Fermi surface plots of (c)  $ZrNiSi$  and (d)  $NbCoSi$ . The electron and hole Fermi surfaces are shown in blue and red, respectively.

between the different elements, we have plotted the electron density isosurfaces. The isosurfaces for  $ZrNiSi$  and  $NbCoSi$  as representatives are shown in Fig. 7, while those of the other compounds are given in the Supplemental Material [27]. From these, we find that the charge density is localized primarily on the  $M$ ,  $T$ , and  $X$  atoms analogous to a charge density distribution usually observed in ionic compounds. However, while on  $M$  the charge density is more spherical; on  $T$  and  $X$  they are pointed towards each other with slight accumulation in between the  $T-X$  bonds. This directional nature of the charge density distribution on  $T$  and  $X$ , and accumulation of electron density in between the bonds, suggests the covalent nature of the bonding between  $T$  and  $X$ . We note that a similar type of bonding is also observed previously for the hH alloys [29–31].

The calculated band structure along the high symmetry directions of the irreducible Brillouin zone and the density of states (DOS) along with their contributions from atomic orbitals of  $M$ ,  $T$ , and  $X$  are shown in Fig. 8, and comparison of the total DOS for all the studied compounds is shown in Fig. 9.

Our results are in good agreement with that reported in literature [6]. The electronic structure of  $NbCoSi$  is shown in Fig. 8(d). All the compounds are metallic. Moreover, all of them except  $ZrNiSb$  exhibit a pseudogaplike feature near the Fermi energy ( $E_F$ ) with a gap size of about 0.1 eV, which is comparable to that previously reported for  $TiNiSi$  [14]. The absence of the pseudogap in  $ZrNiSb$  is due to the extra  $p$  electron added by  $Sb$  to the  $NiSb$  sublattice, without adding any additional states. As a consequence,  $E_F$  is pushed up above the pseudogap, resulting in a relatively large density of states at  $E_F$ , thereby making this system unstable as is evident from the lack of a stoichiometric sample of this compound. The band structures of  $ZrNiSi$ ,  $ZrNiGe$ , and  $HfNiSi$  are very similar, suggesting that replacing Zr with Hf or Si with Ge induces only minor structural changes in terms of their lattice parameters and bond lengths. These changes are not large enough to change their electronic properties significantly.

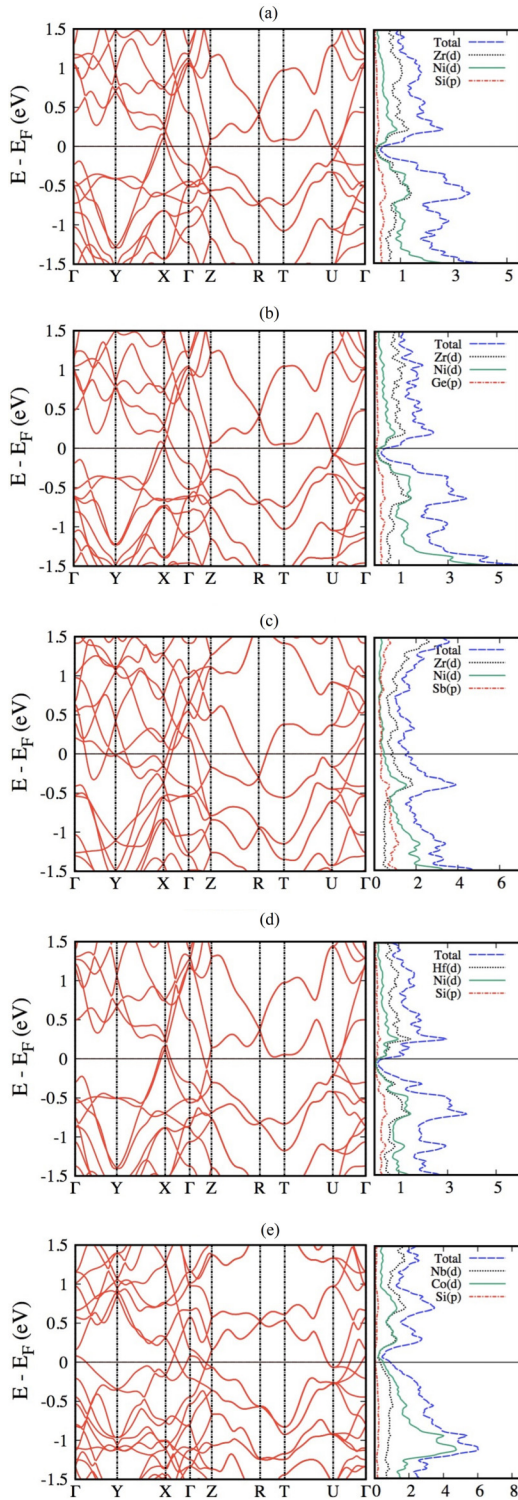


FIG. 8. Band structure and DOS plots of (a) ZrNiSi, (b) ZrNiGe, (c) ZrNiSb, (d) HfNiSi, and (e) NbCoSi.

Hence we anticipate them to also exhibit similar transport properties. For these materials, at  $E_F$  we find electron and hole pockets located around the  $U$  point and  $X$  point of the BZ, respectively. The Fermi surface for ZrNiSi is shown as a representative case in Fig. 7(c). Our calculations suggest that in these materials electrons will be the majority carriers. In

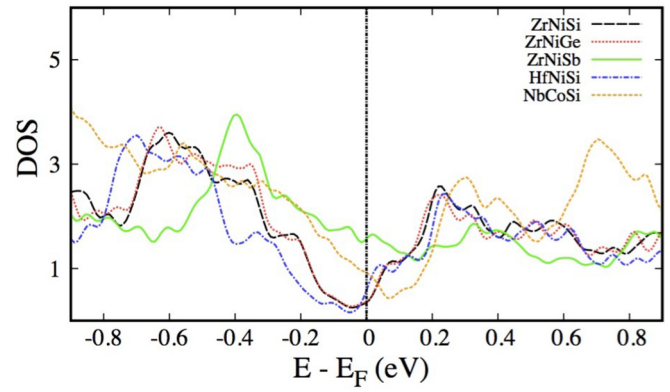


FIG. 9. Comparison of the total DOS for the five compounds: ZrNiSi, ZrNiGe, ZrNiSb, HfNiSi, and NbCoSi.

contrast, in NbCoSi we observe large hole pockets at  $\Gamma$  point along the lines  $\Gamma - Z$  and  $\Gamma - X$ , and electron pockets near  $U$  point of the BZ. The Fermi surface is shown in Fig. 7(d). In this case the hole pockets (red) are significantly larger than the electron pockets (blue). The Fermi energy is below the pseudogap and the holes will be dominant carriers in this case.

In order to understand the difference between the positions of  $E_F$  in ZrNiX ( $X = \text{Si, Ge}$ ) and NbCoSi, though both are iso-electronic, it will be instructive to look into the hybridization of the atomic orbitals. Figures 10(a) and 10(b) show the DOS projected onto the  $d$  orbitals of Zr/Nb,  $d$  orbitals of Ni/Co, and the  $p$  orbitals of Si. Depending on the interactions between the atoms, the DOS can be divided into five regions for simplicity (see Fig. 10). The nature of hybridization between the atomic orbitals in each region can be understood from the integrated local DOS (ILDOS) isosurfaces, which are shown for each region in Fig. 10. As shown, in regions I and II the electronic states result primarily from the hybridization of the Ni/Co  $d$  states with the  $p$  states of Si, resulting in bonding orbitals. In regions III, IV, and V, the dominant contributions come from the  $d$  states of Zr/Nb and Ni/Co. While in region III, the wave functions have larger weight on Ni (Co) atoms than on Zr (Nb) atoms in ZrNiSi (NbCoSi), the reverse is true for region V. In contrast, in region IV, Zr (Nb) and Ni (Co) have similar contributions. In this energy window some hybridization between Nb/Zr  $d$  states and Si  $p$  orbitals remains, as is evident from the ILDOS. We note that similar hybridization has been previously reported for the hH alloys ZrNiSn [32].

Although there are broad similarities between ZrNiSi and NbCoSi, there are also some notable differences. These are (i) the regions I–IV are broader in NbCoSi than in ZrNiSi, (ii) in region III, the contribution from Nb  $d$  states in NbCoSi is more than Zr  $d$  states in ZrNiSi, and (iii) position of  $E_F$  is in region III top in NbCoSi, while it is in region V bottom in ZrNiSi, i.e., the states in region IV are occupied in ZrNiSi, while they are empty in NbCoSi.

The broadening of the bands in NbCoSi can be attributed to the larger overlap of the atomic orbitals. This is in accordance with significantly shorter bonds in NbCoSi compared to ZrNiSi. The difference in the Zr/Nb  $d$  state contributions in region III can be understood in terms of the electronegativity difference (END) between the Nb–Co pair in NbCoSi

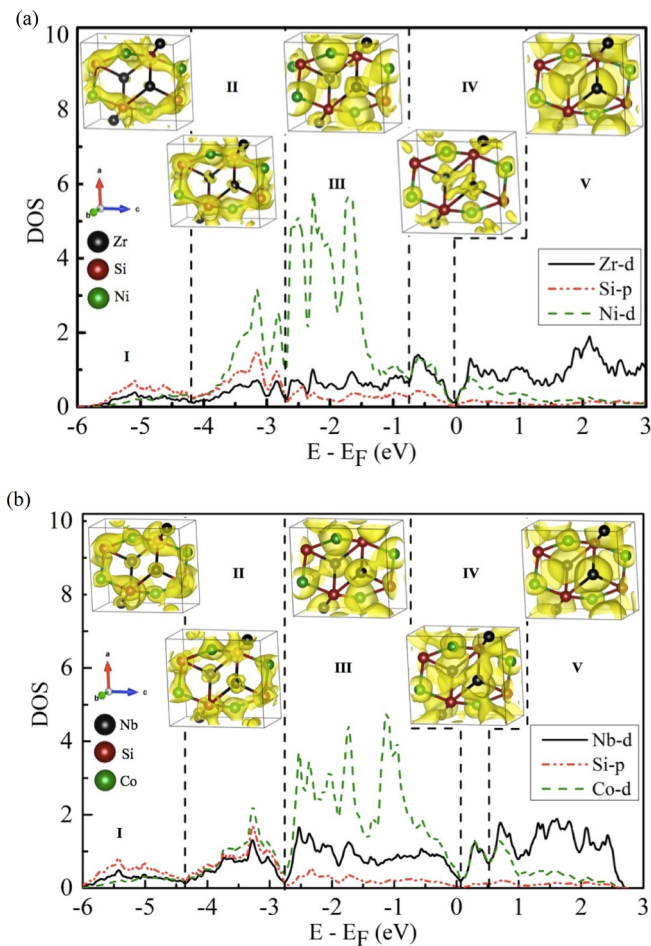


FIG. 10. DOS projected onto the Zr/Nb and Ni/Co  $d$ -states and Si  $p$  states in (a) ZrNiSi and (b) NbCoSi. In each panel, the projected DOS has been divided into five regions. The ILDOS isosurfaces showing the hybridization of the atomic orbitals in each region for the two compounds are shown in the inset. The isovals corresponding to these plots vary between  $0.0121$  and  $0.162 e/\text{\AA}^3$ .

( $\approx 0.28$ ), and the Zr–Ni pair in ZrNiSi ( $\approx 0.57$ ). Since states in region III arise from mixing of  $d$  orbitals of  $M$  and  $T$  elements, a larger END implies that the lower energy states will have larger contribution from the more electronegative element, which in the case of ZrNiSi is Ni.

Finally, the differences in the position of Fermi energy can be understood from the fact that the states in region IV arise due to the hybridization of Zr–Si and Zr–Ni in ZrNiSi (and Nb–Si and Nb–Co in NbCoSi). The ILDOS corresponding to these states (Fig. 10) shows that the hybridization of Zr/Nb– $d$  states with Si– $p$  states results in a bonding type orbital. The corresponding antibonding state lies higher in energy and is not shown in the DOS in Fig. 10. The difference in the energy between the bonding and antibonding hybridized orbitals depends on the END between the hybridizing atoms. As END for Zr–Si and Zr–Ni pairs is more than that for Nb–Si and Nb–Co, the splitting of the bonding and antibonding orbital will be more for ZrNiSi than for NbCoSi. As a result of this, in ZrNiSi (NbCoSi), region IV of the DOS that corresponds to these bonding states is closer to region III (V). Hence these states are occupied in ZrNiSi while empty in NbCoSi,

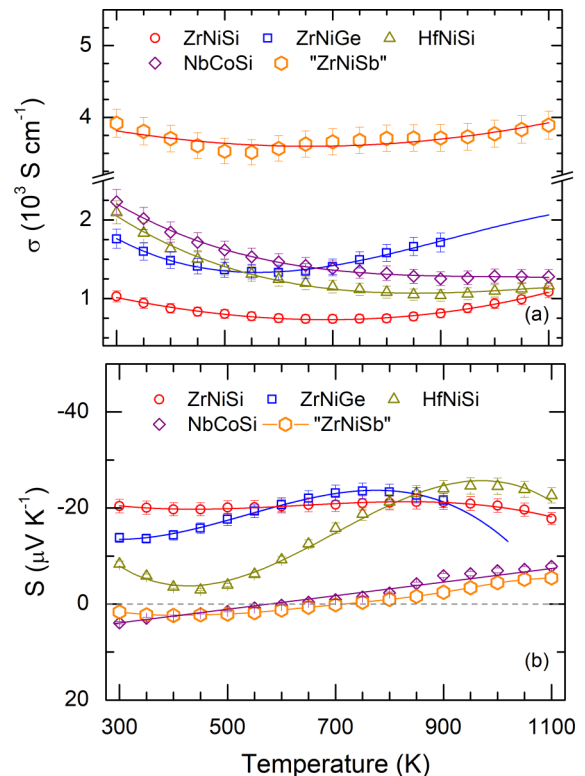


FIG. 11. Temperature variation of (a) electrical conductivity ( $\sigma$ ) and (b) Seebeck coefficient ( $S$ ) for all the studied samples. Here, ‘ZrNiSb’ represents the sample with nominal stoichiometry  $\text{Zr}_{1.05}\text{NiSb}$ . The lines through the data points are a guide to the eye.

resulting in the Fermi level lying at the top of region IV in ZrNiSi but at its bottom in NbCoSi.

## C. Thermoelectric properties

### 1. Electrical transport

**Electrical conductivity.** Figure 11(a) shows the temperature variation of electrical conductivity [ $\sigma(T)$ ]. In all cases, a weak temperature dependent behavior is observed. In ZrNiSi, ZrNiGe, HfNiSi, and NbCoSi (i.e., samples with a pseudogap),  $\sigma$  near room-temperature ranges from  $1000 \text{ S cm}^{-1}$  to  $2000 \text{ S cm}^{-1}$ . Above room temperature  $\sigma$  decreases gradually, and with further heating it either shows a mild upturn (as in ZrNiX for  $X = \text{Si, Ge}$ ) in the range  $600\text{--}700 \text{ K}$  or a tendency towards saturation (as in HfNiSi and NbCoSi). The magnitude of  $\sigma$  and its temperature dependence in ZrNiX ( $X = \text{Si, Ge}$ ) is in good agreement with that reported previously for TiNiSi [14].

In degenerate semiconductors, such as the hH compounds, the upturn in  $\sigma$  is typically attributed to the onset of minority charge carriers at high temperatures. On the other hand, in semimetals both types of charge carriers contribute to the electrical conduction ( $\sigma = \sigma_n + \sigma_p$ ) at any temperature. However, as shown in Sec. III B, the semimetals studied here not only have a pseudogaplike feature in their density of states; they also have majority carrier pockets much larger in volume compared to the minority carrier pockets (see Fig. 7 here and Fig. S5 in the Supplemental Material [27]). Thus the electrical



conductivity of these samples is expected to be mainly due to the majority charge carriers assuming that the mobility  $\mu$  of minority carriers is not drastically high. The decreasing behavior of  $\sigma$  above 300 K, and up to considerably higher temperatures, indeed suggests that the minority contribution remains suppressed until sufficiently high temperatures are reached.

In the antimonide ‘ZrNiSb,’ which has no pseudogap and where DOS at  $E_F$  is at least twice as large,  $\sigma$  at room temperature ( $\approx 4000 \text{ S cm}^{-1}$ ) has been almost fourfold increased compared to ZrNiSi. The temperature dependence of  $\sigma$  is, however, analogous to that of ZrNiSi with minority carrier contribution leading to a shallow minimum at high temperatures.

On qualitative terms the temperature variation of  $\sigma$  in these samples is analogous to the hH compounds as pointed out above; however, the magnitude of  $\sigma$  in undoped hHs is typically of the order of  $100 \text{ S cm}^{-1}$ , which is smaller than that for the compounds studied here. At the same time,  $\sigma$  in these compounds is at least an order of magnitude smaller than for typical intermetallic alloys and compounds [33]. Thus the electrical conductivity of our samples is somewhere between those of degenerate semiconductors and intermetallics.

**Thermopower.** The temperature variation of the Seebeck coefficient ( $S$ ) of our samples is shown in Fig. 11(b).  $S$  displays a weak temperature dependence, and in agreement with the theoretical prediction, near room temperature,  $S$  is negative for ZrNiSi, ZrNiGe, and HfNiSi, and positive for NbCoSi and ZrNiSb.

For ZrNiSi, ZrNiGe, and HfNiSi, the Seebeck coefficient remains negative over the whole temperature range. The average value of  $S$  for these samples ranges from  $10 \mu\text{V K}^{-1}$  to  $20 \mu\text{V K}^{-1}$ . NbCoSi and ‘ZrNiSb’ have a small positive Seebeck coefficient at room temperature which changes sign upon heating above  $\approx 750 \text{ K}$ . The weak modulations of  $S$  with temperature (as in ZrNiSi, ZrNiGe, and HfNiSi) or change of sign (as in NbCoSi and ‘ZrNiSb’) can be attributed to the bipolar nature (i.e., the increasing contribution of the minority charge carriers with temperature). However, interpretation of the variation of  $S$  with temperature in a multiband system is challenging since  $S$  is a complex quantity which is sensitive to several material’s parameters, including the carrier concentration, effective mass, valley degeneracy, and the variation of the electronic density of states at  $E_F$  with energy, which itself may have some temperature dependence.

We now compare the Seebeck coefficient of these materials with the well studied hH compounds. In hH  $M\text{NiSn}$  ( $M = \text{Ti, Zr, and Hf}$ ),  $S$  is reported to be of the order of  $100 \mu\text{V K}^{-1}$  near 300 K, which is almost an order of magnitude higher than what we report here. One reason for this could be the higher electrical conductivity of our samples. However, one should also take into account the fact that hHs have a higher (cubic) crystal symmetry, which leads to a higher valley degeneracy and hence a higher value of the Seebeck coefficient. Finally, the effect of bipolarity in decreasing the average thermopower ( $[S_n\sigma_n + S_p\sigma_p]/[\sigma_n + \sigma_p]$ ) is expected to have more severe consequences for our samples.

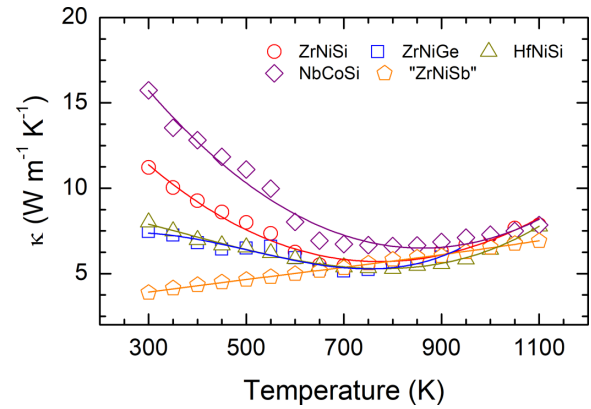


FIG. 12. Temperature variation of thermal conductivity ( $\kappa$ ) of the samples studied here. The legend ‘ZrNiSb’ corresponds to the sample with nominal composition  $\text{Zr}_{1.05}\text{NiSb}$ . Lines through the data points are used as a guide to the eye.

## 2. Thermal conductivity

The thermal conductivity ( $\kappa$ ) of our samples is shown in Fig. 12. With the exception of ‘ZrNiSb’ or  $\text{Zr}_{1.05}\text{NiSb}$ ,  $\kappa$  in all other samples decreases upon heating followed by a slight increase at high temperatures ( $T \sim 700 \text{ K}$ ). Near room temperature,  $\kappa$  is  $\approx 15 \text{ W m}^{-1} \text{ K}^{-1}$  for NbCoSi,  $\approx 11 \text{ W m}^{-1} \text{ K}^{-1}$  for ZrNiSi, and  $\approx 7 \text{ W m}^{-1} \text{ K}^{-1}$  for both ZrNiGe and HfNiSi samples. We note that these values are either comparable to or lower than that previously reported for the hH alloys, including  $M\text{NiSn}$  ( $M = \text{Ti, Zr, and Hf}$ ) and their doped variants [34–39]. The decreasing behavior of  $\kappa$  above room temperature can be attributed to the phonon-phonon scattering processes; the upturn at high temperatures, on the other hand, is likely a consequence of bipolarity. Similar upturn due to the onset of minority carriers has also been reported for the hHs alloys [34–39]. Interestingly, despite being most electrically conducting, the thermal conductivity of ‘ZrNiSb’ is the lowest, close to  $4 \text{ W m}^{-1} \text{ K}^{-1}$  near room temperature, and it also increases almost linearly upon heating, reaching  $7 \text{ W m}^{-1} \text{ K}^{-1}$  at 1100 K, suggesting that the lattice component of  $\kappa$  is heavily suppressed for this sample.

Using the Weidemann-Franz law one can get a tentative estimation of the electronic ( $\kappa_e$ ) and lattice ( $\kappa_l$ ) contributions. The experimental  $\kappa$  can be expressed as an algebraic sum of  $\kappa_e$  and  $\kappa_l$ , i.e.,  $\kappa = \kappa_e + \kappa_l$ . Here,  $\kappa_e = L\sigma T$ , where  $L$  is the Lorentz number. Strictly speaking, we should have also considered the bipolar contribution [14,40]; however, due to some specific features of the electronic structure in these compounds (Sec. III B), including the presence of a pseudogap and relatively larger size of the majority charge carrier pockets (electron in ZrNiSi, ZrNiGe, and HfNiSi and holes in NbCoSi) than the minority carrier pockets (see Fig. 7), the bipolar contribution is expected to be small unless the sample is heated to high temperatures (i.e.,  $T > 700 \text{ K}$  or so). For the purpose of a rough estimate, we take the Lorentz number to be  $2.44 \times 10^{-8} \text{ W } \Omega \text{ K}^{-2}$  as in the metals. This also complies with the fact that, in the degenerate semiconductors, such as

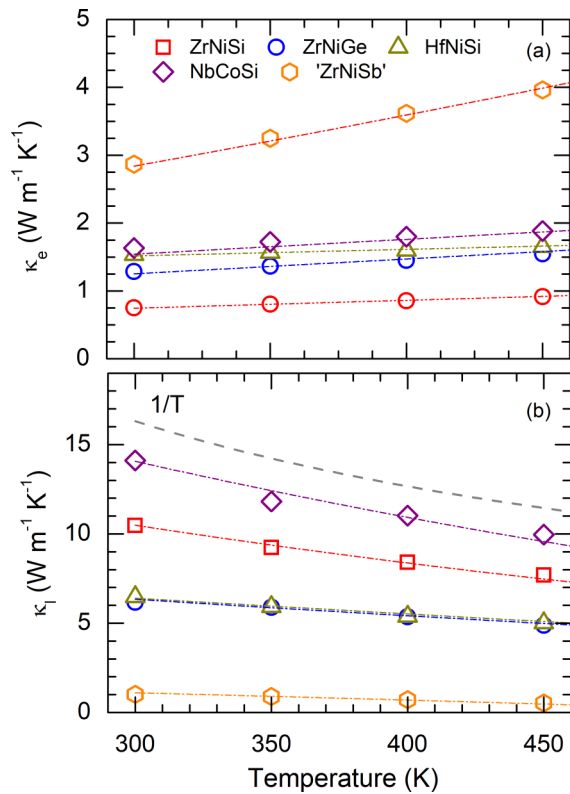


FIG. 13. (a) Electronic ( $\kappa_l$ ) and (b) lattice ( $\kappa_l$ ) thermal conductivity. The lines are used as a guide to the eye. In panel (b), the black dashed line at the top shows the  $1/T$  dependence.

VEC 18 hH alloys, the Lorentz number obtained by a rigorous calculation is typically only slightly smaller than this value.

The temperature variation of  $\kappa_e$  and  $\kappa_l$  thus obtained is shown in Fig. 13. The magnitude of  $\kappa_e$  near 300 K is approximately  $0.75 W m^{-1} K^{-1}$  for ZrNiSi ( $\approx 6\%$  of  $\kappa$ ),  $1.25 W m^{-1} K^{-1}$  for ZrNiGe ( $\approx 17\%$  of  $\kappa$ ),  $1.5 W m^{-1} K^{-1}$  for HfNiSi ( $\approx 20\%$  of  $\kappa$ ),  $1.7 W m^{-1} K^{-1}$  for NbCoSi ( $\approx 10\%$  of  $\kappa$ ), and  $2.9 W m^{-1} K^{-1}$  for 'ZrNiSb' ( $\approx 72\%$  of  $\kappa$ ). Since  $\sigma$  has a weak temperature dependence, in the 300 K to 500 K range,  $\kappa_e = L\sigma T$  shows an increasing behavior roughly proportional to  $T$ .

$\kappa_l$  is plotted in Fig. 13(b). In ZrNiSi and NbCoSi,  $\kappa_l$  follows a  $1/T$  behavior, suggesting the dominance of Umklapp scattering. In ZrNiGe and HfNiSi, the presence of additional scattering modes is also indicated by a slower than  $1/T$  decrease. Going by their stoichiometry as determined using EDX, which is relatively off from the ideal value for these samples, we attribute this to the point defect scattering.

Interestingly, even though 'ZrNiSb' has the highest electrical conductivity, its thermal conductivity is smallest among all the investigated samples, with  $\kappa_l < 1 W m^{-1} K^{-1}$ . To give a perspective on how small this value is, consider the case of hH alloys where such small values are reported only for very carefully prepared nanostructured samples with high grain-boundary scattering and substantial point-mass fluctuations induced by doping of two or three elements [32,41,42]. The thermal diffusivity ( $D$ ) is the measured quantity from which  $\kappa$  is derived; a comparison of  $D$  would help in substantiating this point further. At room temperature  $D$  for

our 'ZrNiSb' sample is  $\approx 1.9 mm^2 s^{-1}$ , which is comparable to a value of  $1.5 mm^2 s^{-1}$  reported for the nanostructured  $Zr_{0.5}Hf_{0.5}CoSb_{0.8}Sn_{0.2}$  [43], which is one of the smallest  $D$  values reported for any hH alloy to the best of our knowledge. Such a low value of  $\kappa_l$  in 'ZrNiSb' is likely due to the presence of high density of structural disorder as shown in Fig. 6. The other factors such as point defect scattering which is expected to be more pronounced here due to off stoichiometry may further contribute to decreasing  $\kappa$ . Finally, the heavier average atomic mass of 'ZrNiSb' compared to other samples is also expected to play a role.

In general, a relatively low-thermal conductivity of these compounds compared to their hH counterparts, despite almost an order of magnitude higher electrical conductivity, is rather interesting, and the role of the chair-shaped ... Si–Ni–Si–Ni ... framework [Fig. 1(b)] in the crystal structure of these compounds, which is known to be one of the factors responsible for its ultralow thermal conductivity of SnSe [7], should also be scrutinized in future.

#### IV. SUMMARY AND CONCLUSIONS

We investigated the phase stability, formation, and thermoelectric properties of ZrNiSi, ZrNiGe, HfNiSi, NbCoSi, and ZrNiSb. All the compounds are shown to crystallize with the orthorhombic TiNiSi structure type. In ZrNiSb, about 5% excess Zr is required to obtain the pure orthorhombic phase.

Our first-principles electronic band structure calculations reveal that these compounds are semimetals with their Fermi surfaces comprised of small electron and hole pockets. The electronic density of states (DOS) present a pseudogap feature with  $E_F$  located either slightly below (ZrNiSi, ZrNiGe, and HfNiSi) or slightly above (NbCoSi) the pseudogap. The position of  $E_F$  with respect to the pseudogap is explained on the basis of the electronegativity difference between the  $M$  and the  $X$  elements in  $MTX$ . In ZrNiSb no pseudogap could be found; however, the DOS at  $E_F$  are only modestly enhanced with respect to the other studied compounds.

The experimental data supports the theoretical findings with electrical conductivity near room temperature ranging from  $\approx 10^3 S cm^{-1}$  to  $\approx 4 \times 10^3 S cm^{-1}$ , which decreases upon heating in compliance with their semimetallic nature. The electrical conductivity of these compounds near 300 K is intermediate between that of the degenerate semiconductors and metallic alloys, as one would expect for a semimetal. The thermopower is negative for ZrNiX ( $X = Si, Ge$ ) and HfNiSe, and positive for NbCoSi and ZrNiSb in agreement with the theoretical results. The average value of the Seebeck coefficient is only about  $10 \mu V K^{-1}$ , which is almost an order of magnitude smaller than is typically reported for the hHs alloys.

The thermal conductivity is found to be generally low for these compounds. In  $Zr_{1.05}NiSb$ , which has the highest electrical conductivity ( $\approx 4000 S cm^{-1}$ ) at 300 K of all the studied compounds, the thermal conductivity is as low as  $\approx 4 W m^{-1} K^{-1}$  at room temperature, which increases slowly upon heating, attaining a value of  $\approx 7 W m^{-1} K^{-1}$  at 1100 K. The lattice contribution for this compound is estimated to be  $< 1 W m^{-1} K^{-1}$ , which is very low. The thermal diffusivity ( $D$ ) of  $Zr_{1.05}NiSb$  at 300 K is almost as small as that reported

for the state-of-the-art nanostructure half-Heusler alloys. The low thermal conductivity, despite a reasonably high electrical conductivity, of the studied compounds is an interesting feature which should invite further investigations. It may be intrinsic, related to the presence of the chair-shaped ... Si-Ni-Si-Ni ... framework in the structure, whose role should be further scrutinized. Additionally, in  $Zr_{1.05}NiSb$ , the high density of structural defects that result due to excess Zr may be important in reducing the lattice thermal conductivity to  $<1 \text{ W m}^{-1} \text{ K}^{-1}$ .

To summarize, the orthorhombic *MTX* compounds studied here show an interesting pseudogaplike feature in their electronic density of states, and their electronic structure is characterized by the presence of electron and hole pockets. They are found to be structurally stable and show a reasonably high electrical conductivity along with very low thermal conductivity. Their utility as thermoelectrics is however limited by their low thermopower. The highest thermoelectric figure of merit ( $zT$ ) is therefore very small

( $\approx 0.015$  at 900 K in  $ZrNiGe$ ). In the future, while it will be interesting to understand why these materials have low thermal conductivity, it may also prove worthwhile to try various doping strategies in order to enhance their Seebeck coefficient.

## ACKNOWLEDGMENTS

S.S. and P.G. gratefully acknowledge financial support from the Department of Science and Technology (DST), India, under the DST-Nanomission Thematic Unite Program (Grant no. SR/NM/TP-13/2016). S.K. acknowledges support from Council of Scientific and Industrial Research (CSIR), India, for the Ph.D. fellowship. A.K. gratefully acknowledges support under Prime Minister's Research Fellows (PMRF) scheme. P.G. would like to acknowledge the Department of Science and Technology, India, Grant No. EMR/2016/005275 for funding.

- 
- [1] S. Ghosh, A. Ghosh, P. Sen, and K. Mandal, *Phys. Rev. Applied* **14**, 014016 (2020).
- [2] Q. Ren, W. D. Hutchison, J. Wang, A. J. Studer, and S. J. Campbell, *Chem. Mater.* **30**, 1324 (2018).
- [3] T. Eriksson, L. Bergqvist, T. Burkert, S. Felton, R. Tellgren, P. Nordblad, O. Eriksson, and Y. Andersson, *Phys. Rev. B* **71**, 174420 (2005).
- [4] M. Marshall, J. Sanford, W. Shelton, and W. Xie, *J. Alloys Compd.* **864**, 158617 (2021).
- [5] Y. Liu, P. Sahoo, J. P. A. Makongo, X. Zhou, S.-J. Kim, H. Chi, C. Uher, X. Pan, and P. F. P. Poudeu, *J. Am. Chem. Soc.* **135**, 7486 (2013).
- [6] B. Singh, X. Zhou, H. Lin, and A. Bansil, *Phys. Rev. B* **97**, 075125 (2018).
- [7] L. Zhao, S. Lo, Y. Zhang, H. Sun, G. Tan, C. Uher, C. Wolverton, V. Dravid, and M. Kanatzidis, *Nature (London)* **508**, 373 (2014).
- [8] S. Guo, T. Jia, and Y. Zhang, *J. Phys. Chem. C* **123**, 18824 (2019).
- [9] J. Carrete, W. Li, N. Mingo, S. Wang, and S. Curtarolo, *Phys. Rev. X* **4**, 011019 (2014).
- [10] Z. Feng, Y. Fu, A. Putatunda, Y. Zhang, and D. J. Singh, *Phys. Rev. B* **100**, 085202 (2019).
- [11] P. R. Raghuvanshi, S. Mondal, and A. Bhattacharya, *J. Mater. Chem. A* **8**, 25187 (2020).
- [12] C. Barreteau, J.-C. Crivello, J.-M. Joubert, and E. Alleno, *ACS Combinatorial Science* **22**, 813 (2020).
- [13] S. Guo, S. Anand, Y. Zhang, and G. J. Snyder, *Chem. Mater.* **32**, 4767 (2020).
- [14] Y. Huang, H. Nagai, K. Hayashi, and Y. Miyazaki, *J. Alloys Compd.* **771**, 111 (2019).
- [15] J. Wang, X.-C. Liu, S.-Q. Xia, and X.-T. Tao, *J. Am. Chem. Soc.* **135**, 11840 (2013).
- [16] G. Snyder and E. Toberer, *Nat. Mater.* **7**, 105 (2008).
- [17] H. Goldsmid, *Introduction to Thermoelectricity*, Springer Series in Materials Science (Springer, Berlin, Heidelberg, 2009).
- [18] S. Guo, Z. Liu, Z. Feng, T. Jia, S. Anand, G. J. Snyder, and Y. Zhang, *J. Mater. Chem. A* **8**, 23590 (2020).
- [19] P. Giannozzi, S. Baroni, N. Bonini, M. Calandra, R. Car, C. Cavazzoni, D. Ceresoli, G. L. Chiarotti, M. Cococcioni, I. Dabo, A. D. Corso, S. de Gironcoli, S. Fabris, G. Fratesi, R. Gebauer, U. Gerstmann, C. Gougousis, A. Kokalj, M. Lazzeri, L. Martin-Samos, N. Marzari, F. Mauri, R. Mazzarello, S. Paolini, A. Pasquarello, L. Paulatto, C. Sbraccia, S. Scandolo, G. Sclauzero, A. P. Seitsonen, A. Smogunov, P. Umari, and R. M. Wentzcovitch, *J. Phys.: Condens. Matter* **21**, 395502 (2009).
- [20] P. Giannozzi, O. Andreussi, T. Brumme, O. Bunau, M. Buongiorno Nardelli, M. Calandra, R. Car, C. Cavazzoni, D. Ceresoli, M. Cococcioni *et al.*, *J. Phys.: Condens. Matter* **29**, 465901 (2017).
- [21] D. Vanderbilt, *Phys. Rev. B* **41**, 7892 (1990).
- [22] J. P. Perdew, K. Burke, and M. Ernzerhof, *Phys. Rev. Lett.* **77**, 3865 (1996).
- [23] H. J. Monkhorst and J. D. Pack, *Phys. Rev. B* **13**, 5188 (1976).
- [24] S. J. Crerar and A. Mar, *J. Solid State Chem.* **177**, 2523 (2004).
- [25] T. Harmening, H. Eckert, C. M. Fehse, C. P. Sebastian, and R. Pöttgen, *J. Solid State Chem.* **184**, 3303 (2011).
- [26] G. A. Landrum, R. Hoffmann, J. Evers, and H. Boysen, *Inorg. Chem.* **37**, 5754 (1998).
- [27] See Supplemental Material at <http://link.aps.org/supplemental/10.1103/PhysRevMaterials.5.085406> for Figs. S1, S2, S3, S4, and S5 and Table T1.
- [28] W. G. Zeier, S. Anand, L. Huang, R. He, H. Zhang, Z. Ren, C. Wolverton, and G. J. Snyder, *Chem. Mater.* **29**, 1210 (2017).
- [29] L. Offernes, P. Ravindran, and A. Kjekshus, *J. Alloys Compd.* **439**, 37 (2007).
- [30] C. Felser, L. Wollmann, S. Chadov, G. H. Fecher, and S. S. P. Parkin, *APL Mater.* **3**, 041518 (2015).

- [31] C. Li, Y. Zhao, B. Chi, Y. Gong, and C. Sun, *Computational Condensed Matter* **1**, 8 (2014).
- [32] W. Zeier, J. Schmitt, G. Hautier, U. Aydemir, Z. Gibbs, C. Felser, and G. Snyder, *Nat. Rev. Mater.* **1**, 16032 (2016).
- [33] R. Dremov, N. Koblyuk, Y. Mudryk, L. Romaka, and V. Sechovský, *J. Alloys Compd.* **317-318**, 293 (2001), The 13th International Conference on Solid Compounds of Transition Elements.
- [34] S. Sakurada and N. Shutoh, *Appl. Phys. Lett.* **86**, 082105 (2005).
- [35] Y. W. Chai, T. Oniki, T. Kenjo, and Y. Kimura, *J. Alloys Compd.* **662**, 566 (2016).
- [36] J. Schmitt, Z. Gibbs, J. Snyder, and C. Felser, *Mater. Horiz.* **2**, 68 (2014).
- [37] Q. Shen, L. Chen, T. Goto, T. Hirai, J. Yang, G. P. Meisner, and C. Uher, *Appl. Phys. Lett.* **79**, 4165 (2001).
- [38] W. Xie, A. Weidenkaff, X. Tang, Q. Zhang, J. Poon, and T. M. Tritt, *Nanomaterials* **2**, 379 (2012).
- [39] W. Wong-Ng, J. W. Lynn, Q. Huang, C. M. Brown, J. A. Kaduk, and G. Joshi, *Appl. Phys. Lett.* **107**, 213901 (2015).
- [40] S. Wang, J. Yang, T. Toll, J. Yang, W. Zhang, and X. Tang, *Sci. Rep.* **5**, 10136 (2015).
- [41] T. Zhu, C. Fu, H. Xie, Y. Liu, and X. Zhao, *Adv. Energy Mater.* **5**, 1500588 (2015).
- [42] S. Chen and Z. Ren, *Mater. Today* **16**, 387 (2013).
- [43] X. Yan, G. Joshi, W. Liu, Y. Lan, H. Wang, S. Lee, J. W. Simonson, S. J. Poon, T. M. Tritt, G. Chen, and Z. F. Ren, *Nano Lett.* **11**, 556 (2011).